

Supporting Information

Probing Evolution of Twist-Angle-Dependent Interlayer Excitons in MoSe₂/WSe₂ van der Waals Heterostructures

Pramoda K. Nayak,^{†,‡} Yevhen Horbatenko,[§] Seongjoon Ahn,^{†,‡} Gwangwoo Kim,^{†,‡}
Jae-Ung Lee,^{||} Kyung Yeol Ma,^{†,‡} A-Rang Jang,^{†,‡} Hyunseob Lim,[⊥] Dogyeong
Kim,[#] Sunmin Ryu,[#] Hyeonsik Cheong,^{||} Noejung Park,^{*,§,∇} and Hyeon Suk
Shin^{*,†,‡,§}

[†]Department of Energy Engineering and Department of Chemistry, [‡]Low Dimensional Carbon
Materials Center, and [∇]Department of Physics, Ulsan National Institute of Science and
Technology (UNIST), 50 UNIST-gil, Ulsan 44919, Republic of Korea

[§]Center for Multidimensional Carbon Materials (CMCM), Institute of Basic Science (IBS),
Ulsan 44919, Republic of Korea

^{||}Department of Physics, Sogang University, Seoul 04107, Republic of Korea

[⊥]Department of Chemistry, Chonnam National University, Gwangju 61186, Republic of Korea

[#]Department of Chemistry, Pohang University of Science and Technology (POSTECH), Pohang,
Gyeongbuk790-784, Republic of Korea

* E-mail: shin@unist.ac.kr (HSS) and noejung@unist.ac.kr (NP)

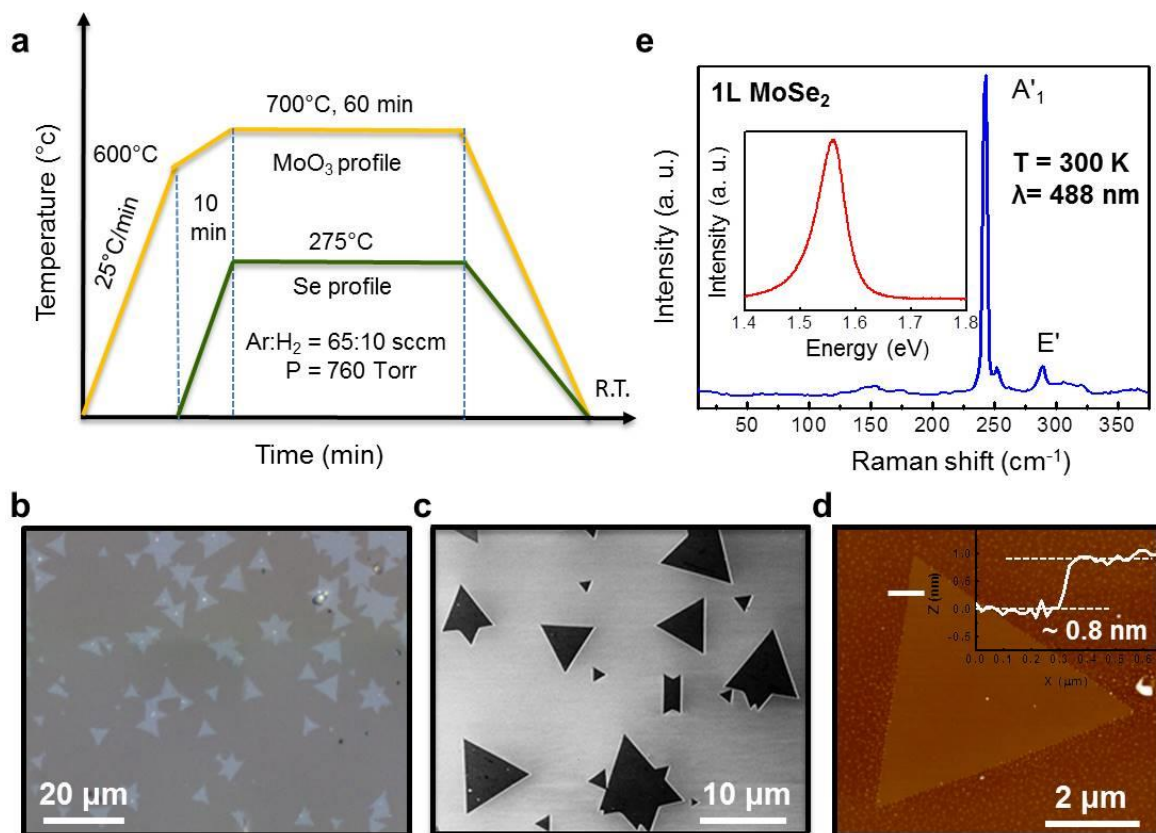


Figure S1. Growth process and characterization of monolayer MoSe₂. (a) Schematic of MoSe₂ growth process using APCVD. The temperature profiles of precursor powders and gas flow rates are displayed in the figure. (b) OM image of as prepared MoSe₂ grains on sapphire substrate. The grains are mostly triangular but some truncated triangular grains are also present. (c) SEM image of a triangular grains showing very sharp edge, which implies good crystallinity of prepared sample. (d) AFM image with height profile of a triangular grain, showing a step height of ~ 0.8 nm corresponds to monolayer MoSe₂ thickness. (e) Raman characterization of a triangular MoSe₂ flake using 488 nm laser showing the characteristics Raman vibration modes A₁' at 240 cm⁻¹ (out of plane mode) and E' at 287 cm⁻¹ (in plane mode). The absence of the layer number sensitive mode A₂'' at 353 cm⁻¹ confirms that prepared MoSe₂ flakes are monolayer. The PL spectrum exhibits peak at 1.56 eV (shown as inset), which is the characteristics of monolayer MoSe₂.

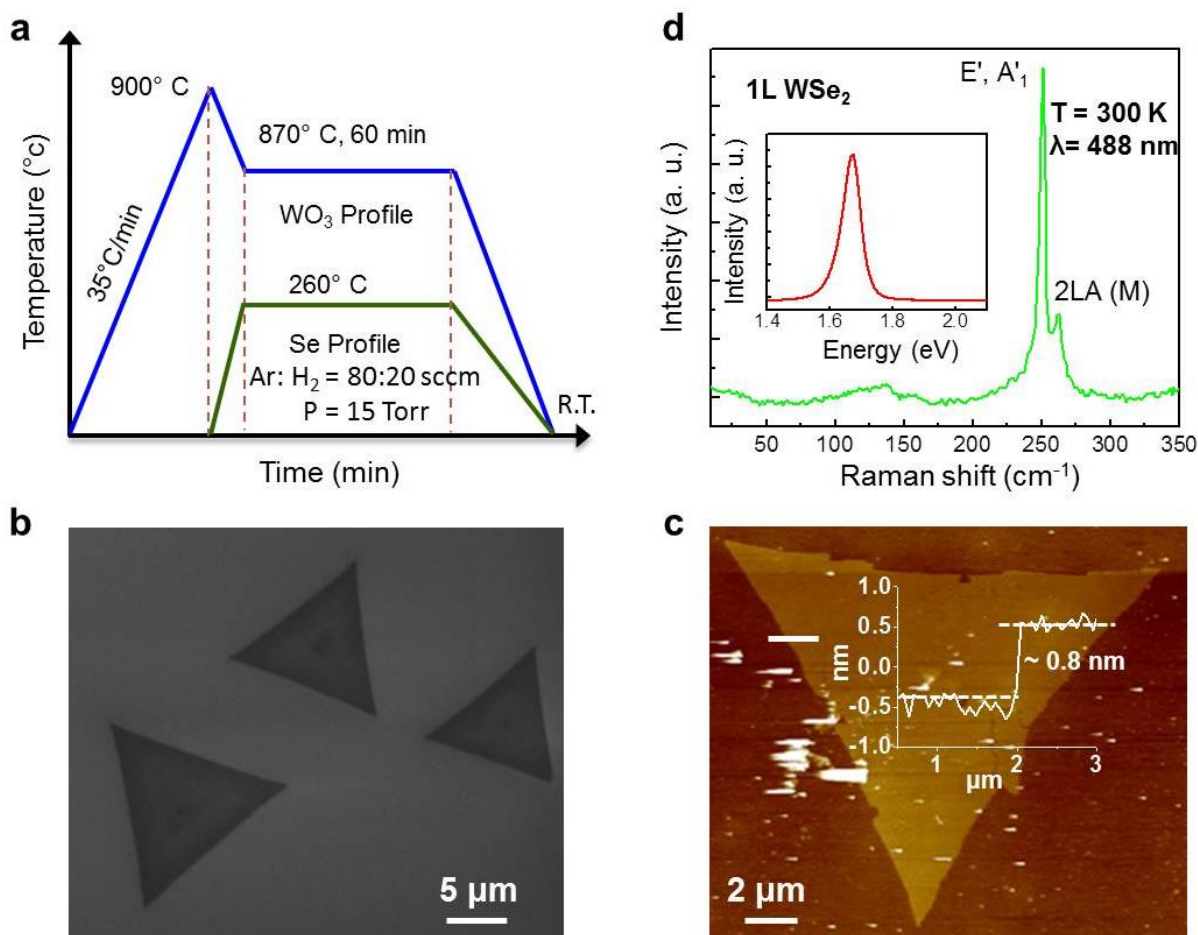


Figure S2. Growth process and characterization of monolayer WSe₂. (a) Schematic of MoSe₂ growth process using LPCVD. The temperature profiles of precursor powders and gas flow rates are displayed in the figure. (b) SEM image of triangular WSe₂ flakes showing very sharp edge, which implies good crystallinity of prepared sample. (c) AFM image with height profile of a WSe₂ flake, showing a step height of ~ 0.8 nm corresponds to monolayer WSe₂ thickness. (d) Raman characterization of a WSe₂ flake using 488 nm laser showing the characteristics Raman vibration modes (E', A₁') at 250 cm⁻¹ and 2LA (M) mode at 262 cm⁻¹. The absence of the layer number sensitive mode A₂' at 309 cm⁻¹ confirms that prepared WSe₂ flakes are monolayer. The PL spectrum exhibits peak at 1.66 eV (shown as inset), which is the characteristics of monolayer WSe₂.

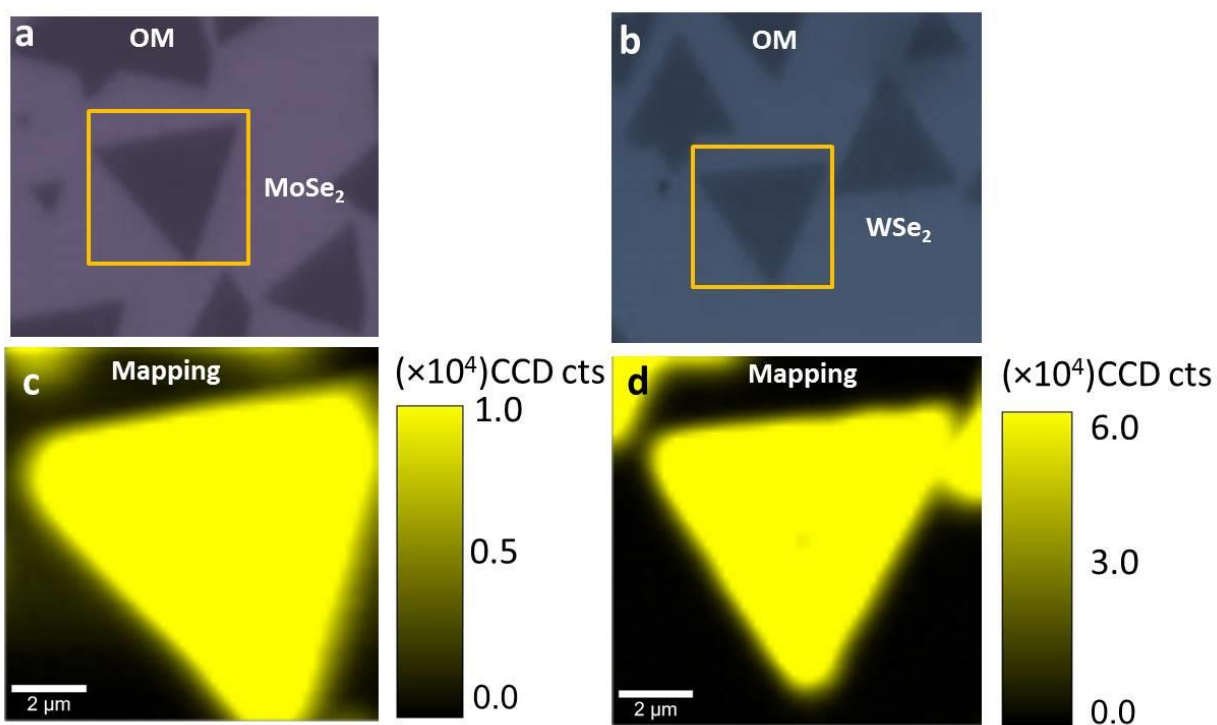


Figure S3. PL mapping of CVD grown MoSe₂ and WSe₂ monolayers on sapphire substrate. OM images of monolayer (a) MoSe₂ and (b) WSe₂. (c, d) PL mapping images of monolayer flakes in the marked regions (a, b) showing uniform PL intensity within the flakes.

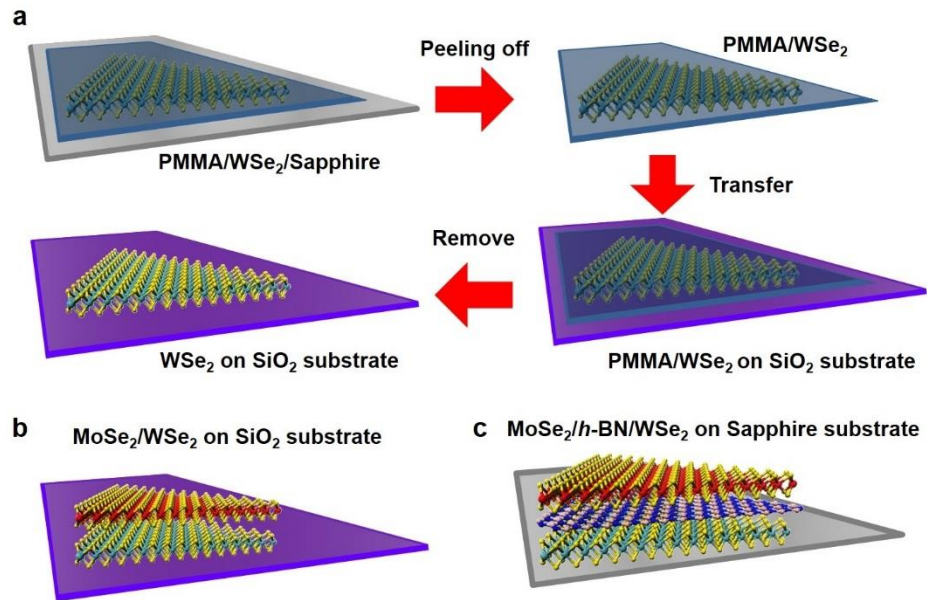


Figure S4. Schematics of MoSe₂/WSe₂ HSs transfer Process. (a) Transfer of as grown WSe₂ from sapphire onto SiO₂ substrate using mechanical peeling and PMMA assisted transfer process. (b) MoSe₂/WSe₂ HS on SiO₂ substrate employing the same transfer process (a), in which WSe₂/SiO₂ is used as substrate instead of pure SiO₂. (c) MoSe₂/h-BN/WSe₂ HS on sapphire substrate. This HS is formed by transferring *h*-BN onto as grown WSe₂/sapphire using bubbling transfer followed by MoSe₂ layer onto it using same transfer process shown in (a). It can be noted that *h*-BN inserted HS has been prepared directly on sapphire substrate in order to reduce the number of transfer steps.

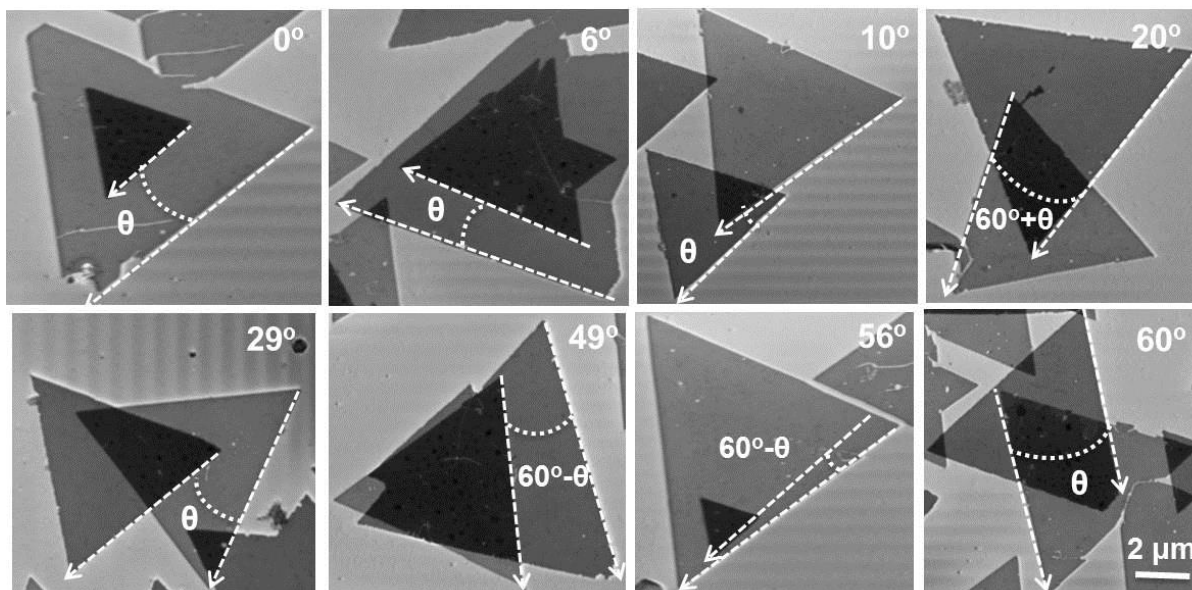


Figure S5. SEM characterization of MoSe₂/WSe₂ HSs. SEM images of MoSe₂/WSe₂ HSs with variety of twist angles in the range $0^\circ \leq \theta \leq 60^\circ$. The flakes with lower contrast are the WSe₂ layer (bottom layer) and with higher contrast are MoSe₂ layer (top layer). In some places, top layer is perfectly overlapped with bottom layer, where as in some places, it is partially overlapped. Twist angle (θ) has been determined by considering the clockwise orientation of the top MoSe₂ triangle with respect to bottom WSe₂ triangle with an error of about 2° . Due to three fold symmetry, the maximum angle is 60° between the two triangles. When the angle exceeds 60° or lags 0° , it is counted as $(60^\circ + \theta)$ or $(60^\circ - \theta)$, where θ is considered as the angle between the two layers. The error has been determined by the differences of the three twist angles determined from each edge (total three edges) in two triangles.

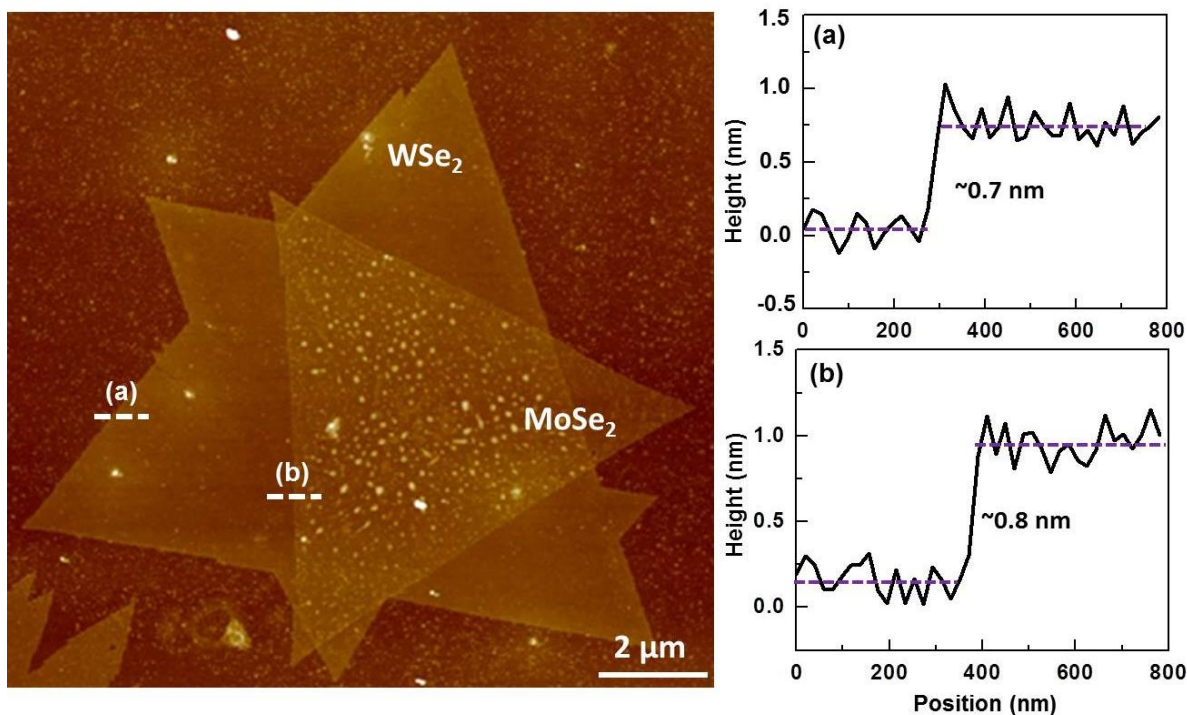


Figure S6. AFM characterization of an MoSe₂/WSe₂ HS. Typical AFM height topographies of a MoSe₂/WSe₂ HS. An edge step height ~ 0.7 nm at the interface of Si substrate-bottom layer (a) and ~ 0.8 nm at the interface of bottom layer-top layer (b) corresponds to thickness of monolayer WSe₂ and MoSe₂/WSe₂. It is observed that the interface between the two layers is clean, apart from some bubbles and wrinkles trapped during the transfer process.^{1,2} These bubbles and wrinkles are common in assembled vdW HSs,¹ which does not affect the vdW HSs' properties.² These are responsible for slight change in crystal edge direction due to puckering and strain. Therefore, there can be an error in the estimation of twist angle in assembled HSs up to 5° reported by Liu *et al.*³ In our study, the error in the twist angle determination is about 2° .

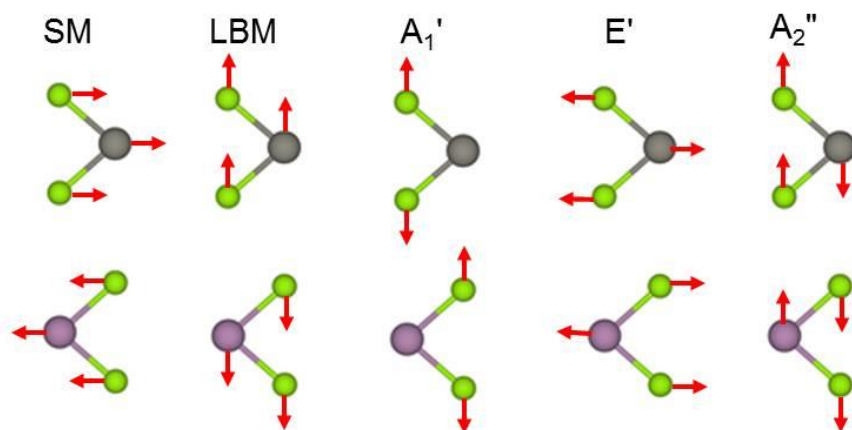


Figure S7. Schematic of Raman Modes in MoSe₂/WSe₂ heterostructure. Shear mode (SM) and layer breathing mode (LBM) observed in the frequency range (10-40 cm⁻¹) are the low frequency Raman mode and other normal modes A₁' , E' observed in the frequency range (200-300 cm⁻¹) are the high frequency Raman active modes. A₂'' is the higher order inactive mode for monolayers. The arrows represent direction of vibrations of constituent atoms.

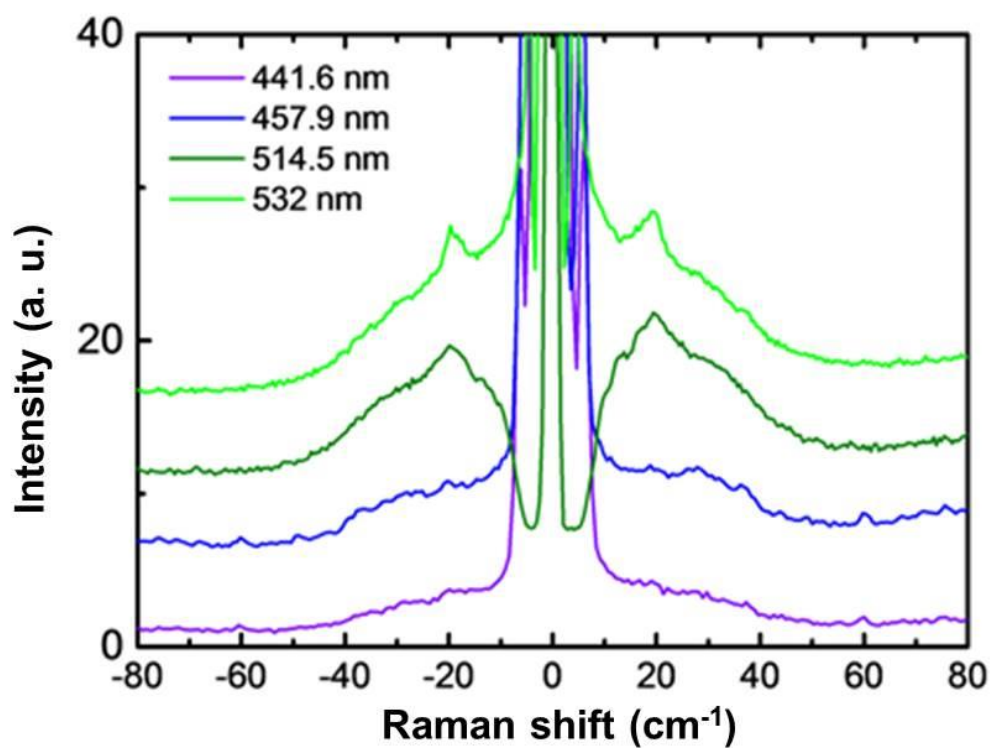


Figure S8. Low Frequency Raman spectra of mechanically exfoliated monolayer WSe₂ with four different excitation energies, *i.e.* 441.6 nm (pink), 457.9 nm (blue), 514.5 nm (red), and 532 nm (green). An unknown peak is observed near 20 cm⁻¹ for 532 nm and 514.5 nm excitations and is absent for 441.6 nm, 457.9 nm excitations due to resonant effect.

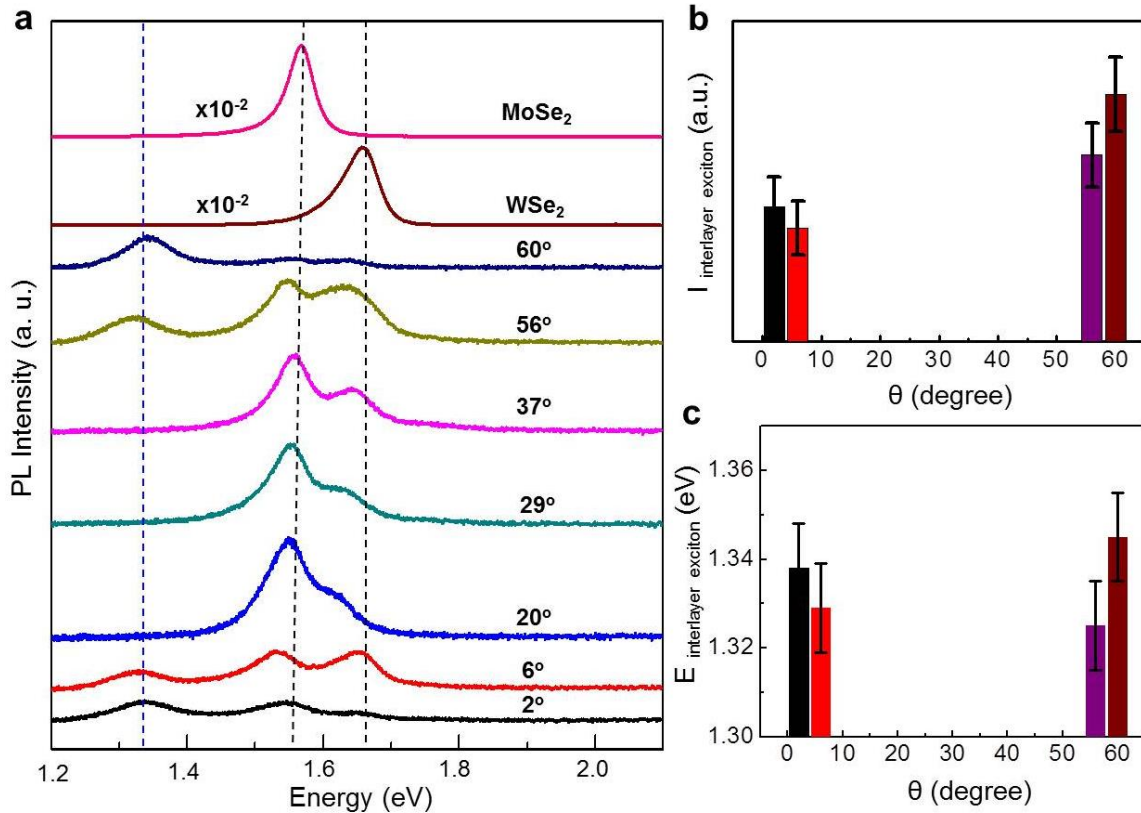


Figure S9. PL analysis of another reverse HS sample. (a) Room temperature PL spectra of monolayered MoSe₂, monolayered WSe₂ and their reverse HSs (WSe₂/MoSe₂) for various twist angles ($2^\circ \leq \theta \leq 60^\circ$) under 50 μ W laser excitation at 2.54 eV (488 nm laser). The direct excitonic peak positions for MoSe₂ (1.57 eV) and WSe₂ (1.66 eV) are marked with vertical black dashed lines. A low energy peak was observed at ~ 1.35 eV for a few twist angles; it is marked with a blue dashed line. (b) Intensity of the interlayer exciton peak *versus* the twist angle. (c) Energy of the interlayer exciton peak *versus* the twist angle. The error bar has been determined by considering three different samples at each angle.

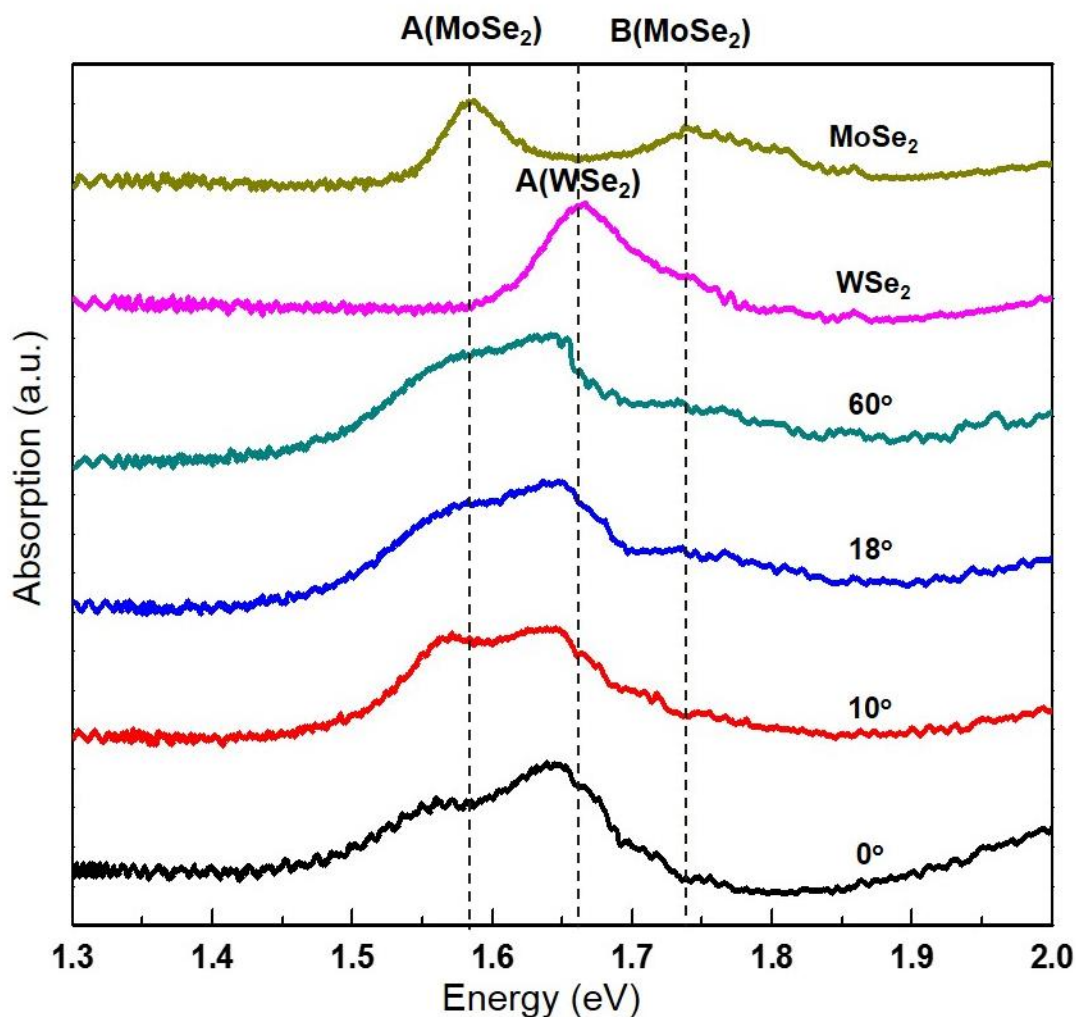


Figure S10. Absorption spectra of monolayer MoSe_2 , WSe_2 , and their vdW HSs ($\text{WSe}_2/\text{MoSe}_2$) with various twist angles ($0^\circ \leq \theta \leq 60^\circ$) prepared on sapphire substrate by micro-UV/Vis spectroscopy at room temperature. The direct excitonic peak positions for MoSe_2 and WSe_2 are marked with vertical black dashed lines. The interlayer exciton peak at low energy is absent since the probability for the interlayer absorption (indirect transition) is very low at room temperature, as predicted theoretically by Komsa *et al.*⁴ The exciton peaks of HSs show red-shift, compared to those of monolayers, which is possibly due to the reduction of dielectric screening as reported in heterobilayers and homobilayers by Yu *et al.*⁵

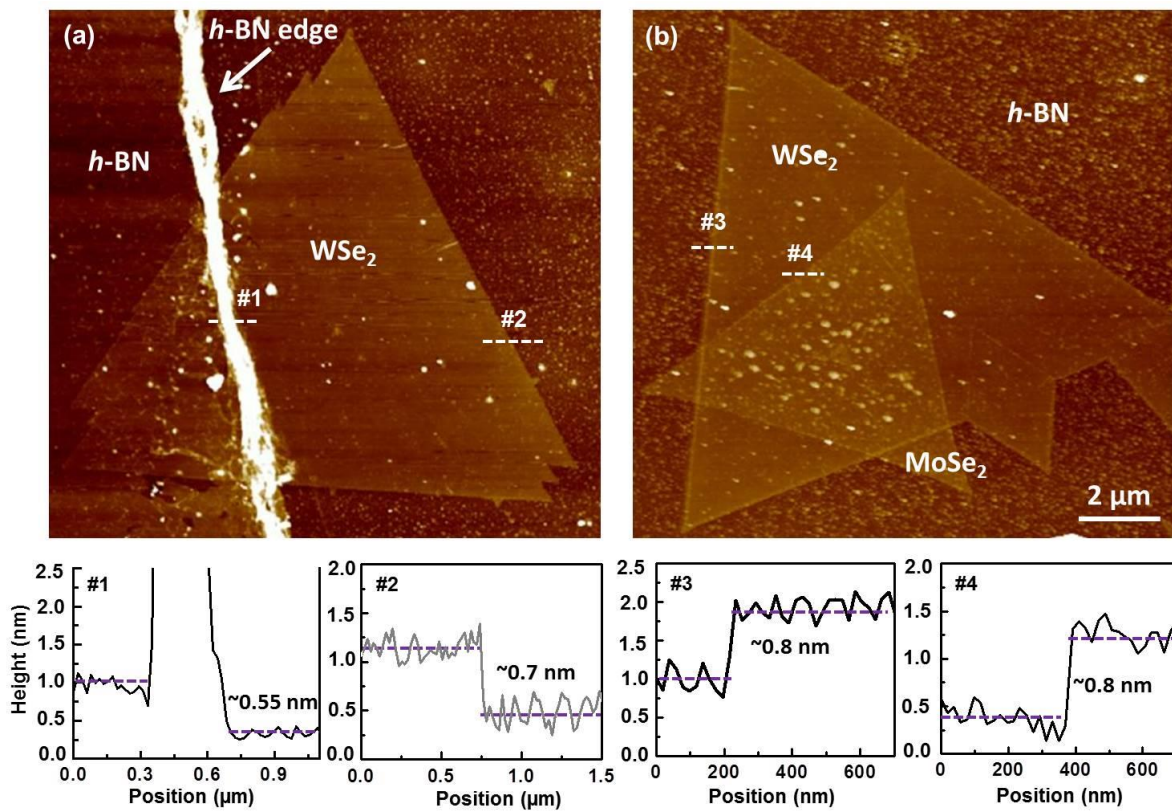


Figure S11. AFM image of (a) 1L *h*-BN transferred on WSe_2 / sapphire and (b) an $MoSe_2/1L$ *h*-BN/ WSe_2 HS flake. The bottom panel shows the representative height profiles of four interfaces in region 1, 2, 3 and 4 respectively.

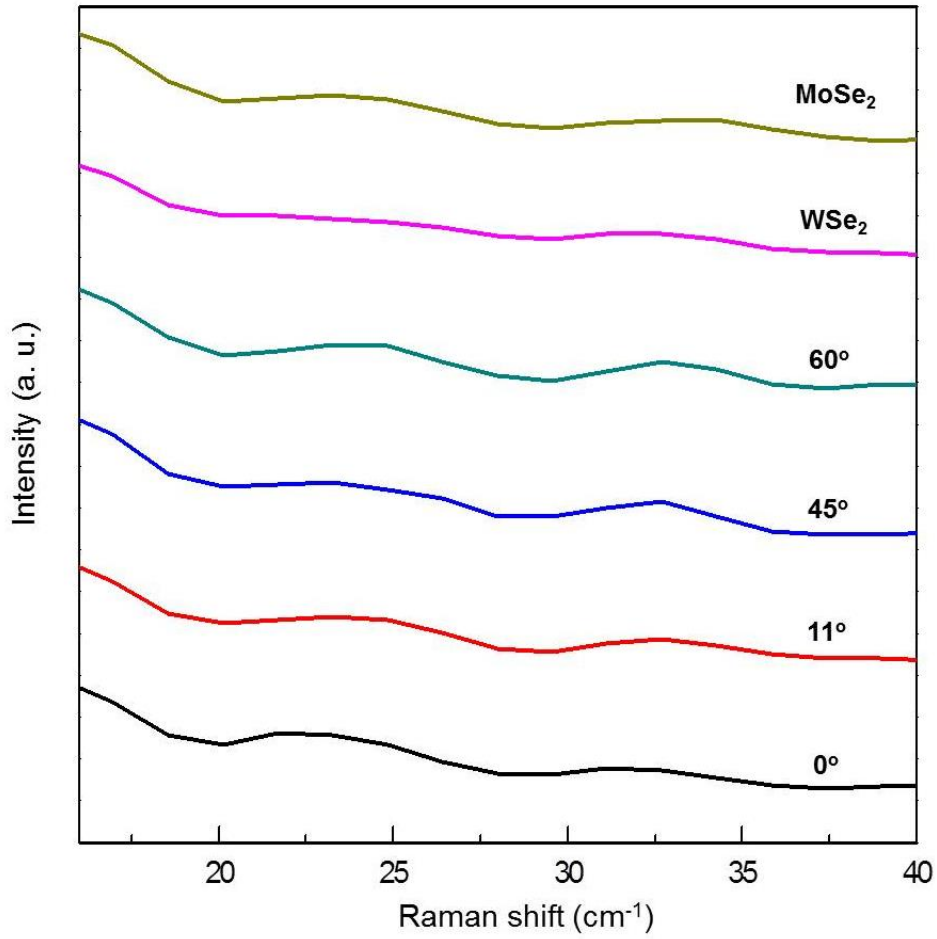


Figure 12. Low frequency Raman spectra for *h*-BN inserted MoSe₂/WSe₂ HS measured for various twist angles ($0^\circ \leq \theta \leq 60^\circ$) under 50 μ W laser excitation at 2.54 eV (488 nm laser). In the low frequency region, the HSs do not show any vibrational modes and spectra behave similar to that of MoSe₂ and WSe₂ monolayers.

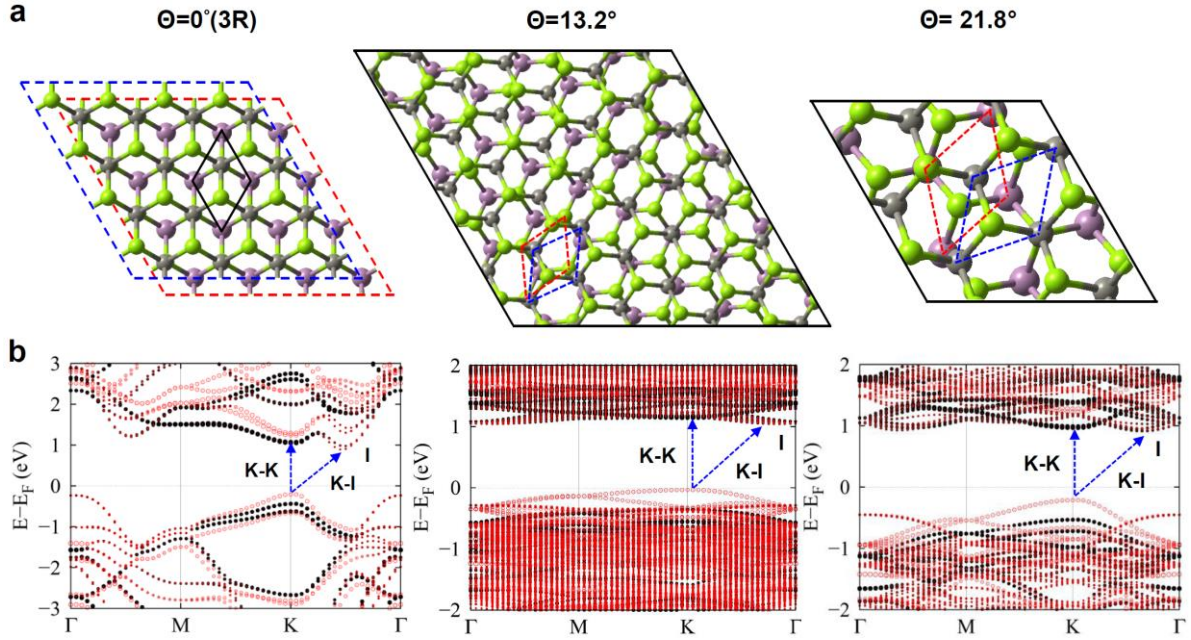


Figure 13. Electronic band structure evolution in MoSe₂/WSe₂ HS. (a) Optimized geometries of HSs with different twist angles ($\theta = 0^\circ$, 13.2° , and 21.8°). The gray, purple, and green balls represent Mo, W, and Se atoms, respectively. The black solid line represents the unit cells used in the computation. The dashed diamonds (red and blue) in the unit cell for the case of $\theta = 13.2^\circ$ and 27.8° indicate the minimal unit cell of each monolayer. (b) DFT-calculated band structures along the Brillouin zone path Γ -M-K- Γ of the lattice depicted in (a). Both the indirect gap between the band extremes K and Γ and the direct gap at K are highlighted by blue dashed arrows. The contributions of the MoSe₂ monolayer and the WSe₂ monolayer are represented by the sizes of the black circles and red circles, respectively. The band plot for the case of $\theta = 13.2^\circ$ and 27.8° contains more bands due to the Brillouin zone folding of the larger supercell.

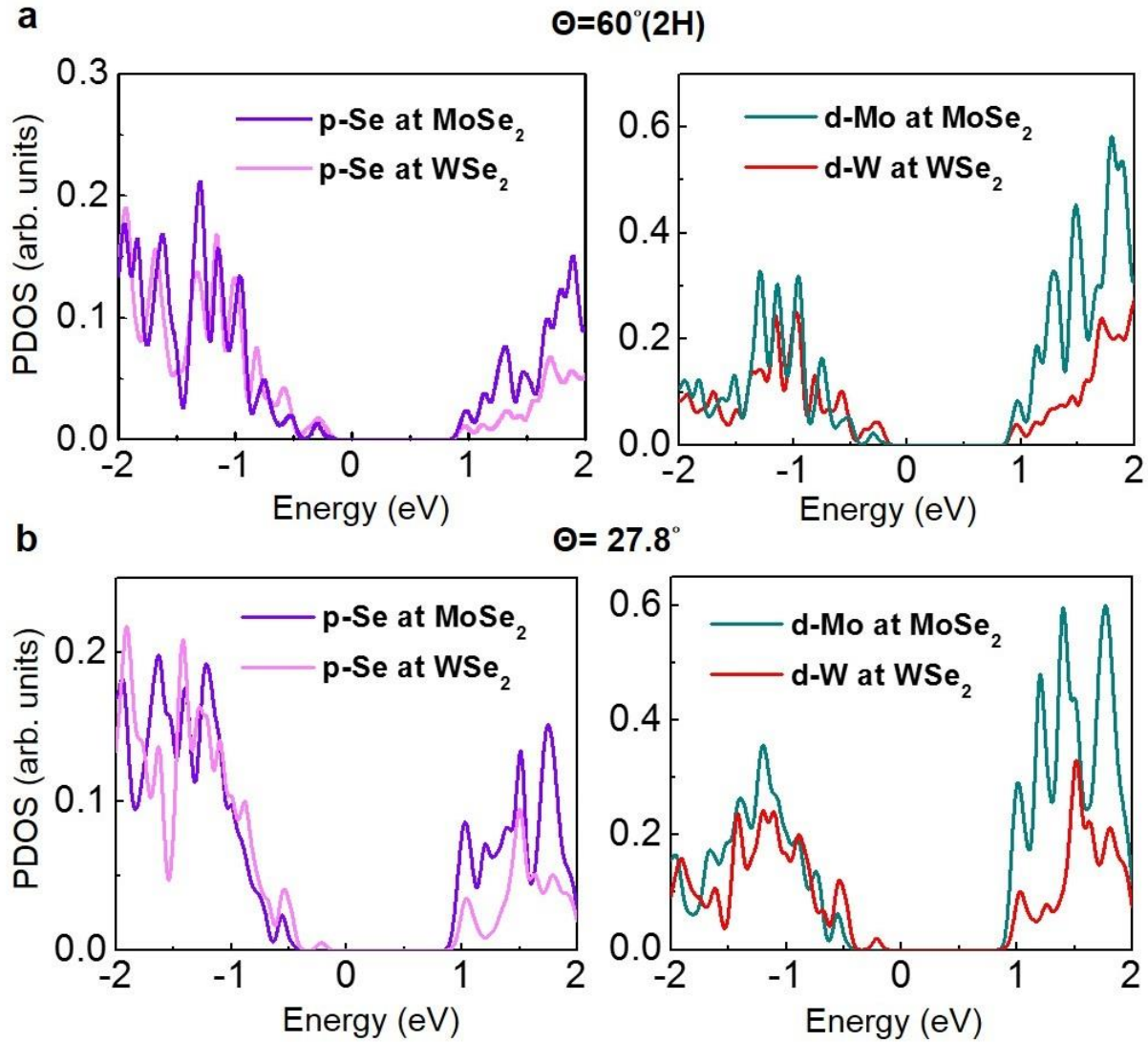


Figure S14. PDOS of some MoSe₂/WSe₂ HS. (a) PDOS for $\theta=60^\circ$ HS shows density of states for p-electrons of the Se atoms at each of the layers (left panel) and for d-electrons of Mo and W at each of the layers (right panel). (b) PDOS for $\theta=27.8^\circ$ HS shows density of states for p-electrons of the Se atoms at each of the layers (left panel) and for d-electrons of Mo and W at each of the layers (right panel).

To analyze the orbital contribution from each element we calculated projected density of states considering p-electrons of Se and d-electrons of the transition metals. As shown in Figure S14, the dominant contribution to the states that are close to the top of the valence band arises from d-orbitals of W and p-orbitals of Se from WSe₂ layer, whereas d-orbitals of Mo and p-orbitals of Se from MoSe₂ layer mainly contribute to the states at the bottom of the conduction band.

Supplementary References

- (1) Chiu, M. H.; Li, M. Y.; Zhang, W. J.; Hsu, W. T.; Chang, W. H.; Terrones, M.; Terrones, H.; Li, L. J. Spectroscopic Signatures for Interlayer Coupling in MoS₂-WSe₂ van der Waals Stacking. *ACS Nano* **2014**, *8*, 9649-9656.
- (2) van der Zande, A. M.; Kunstmann, J.; Chernikov, A.; Chenet, D. A.; You, Y. M.; Zhang, X. X.; Huang, P. Y.; Berkelbach, T. C.; Wang, L.; Zhang, F. et al. Tailoring the Electronic Structure in Bilayer Molybdenum Disulfide *via* Interlayer Twist. *Nano Lett.* **2014**, *14*, 3869-3875.
- (3) Lui, C. H.; Ye, Z. P.; Ji, C.; Chiu, K. C.; Chou, C. T.; Andersen, T. I.; Means-Shively, C.; Anderson, H.; Wu, J. M.; Kidd, T. et al. Observation of Interlayer Phonon Modes in van der Waals Heterostructures. *Phys. Rev. B: Condens. Matter Mater. Phys.* **2015**, *91*, 165403.
- (4) Komsa, H. P.; Krashennnikov, A. V. Electronic Structures and Optical Properties of Realistic Transition Metal Dichalcogenide Heterostructures from First Principles. *Phys. Rev. B: Condens. Matter Mater. Phys.* **2013**, *88*, 085318
- (5) Yu, Y. F.; Hu, S.; Su, L. Q.; Huang, L. J.; Liu, Y.; Jin, Z. H.; Purezky, A. A.; Geohegan, D. B.; Kim, K. W.; Zhang, Y. et al. Equally Efficient Inter Layer Exciton Relaxation and Improved Absorption in Epitaxial and Nonepitaxial MoS₂/WS₂ Heterostructures. *Nano Lett.* **2015**, *15*, 486-491.